

RESEARCH ARTICLE

PLANT SCIENCE

Direct pathogen-induced assembly of an NLR immune receptor complex to form a holoenzyme

Shoucai Ma^{1*}, Dmitry Lapin^{2*}, Li Liu^{2*}, Yue Sun^{1*}, Wen Song^{3*}, Xiaoxiao Zhang¹, Elke Logemann², Dongli Yu^{2,3}, Jia Wang¹, Jan Jirschitzka³, Zhifu Han¹, Paul Schulze-Lefert^{2,4,†}, Jane E. Parker^{2,4,†}, Jijie Chai^{1,2,3,4,†}

Direct or indirect recognition of pathogen-derived effectors by plant nucleotide-binding leucine-rich repeat (LRR) receptors (NLRs) initiates innate immune responses. The *Hyaloperonospora arabidopsidis* effector ATR1 activates the N-terminal Toll–interleukin-1 receptor (TIR) domain of *Arabidopsis* NLR RPP1. We report a cryo–electron microscopy structure of RPP1 bound by ATR1. The structure reveals a C-terminal jelly roll/Ig-like domain (C-JID) for specific ATR1 recognition. Biochemical and functional analyses show that ATR1 binds to the C-JID and the LRRs to induce an RPP1 tetrameric assembly required for nicotinamide adenine dinucleotide hydrolase (NADase) activity. RPP1 tetramerization creates two potential active sites, each formed by an asymmetric TIR homodimer. Our data define the mechanism of direct effector recognition by a plant NLR leading to formation of a signaling-active holoenzyme.

Intracellular nucleotide-binding leucine-rich repeat immune receptors (NLRs) have evolved independently in plants and animals to detect pathogen disturbance. Plant sensor NLRs are classified into two main groups that are defined by different N-terminal domains: a coiled-coil (CC) domain in CC-NLRs (CNLs) and a Toll–interleukin-1 receptor (TIR) domain in TIR-NLRs (TNLs). Direct or indirect recognition of pathogen effector proteins by plant NLRs triggers an immune response termed effector-triggered immunity (1–6), often characterized by rapid host cell death (a hypersensitive response) at sites of attempted infection. In addition to the C-terminal LRR domain, non-canonical integrated domains of plant NLRs play a critical role in conferring specific effector recognition (7). Although modes of effector recognition vary, ligand sensing is widely believed to induce oligomerization of NLRs for signaling. For example, a recent structural study of the CNL ZAR1 in *Arabidopsis* showed that the ZAR1 resistosome induced by bacterial effector AvrAC assumes a wheel-like structure similar to that of NLR inflammasomes in animals (8). A body of evidence suggests that the CC domains of CNLs and the TIR domains of TNLs mediate

signaling upon NLR activation (9–14). A TIR domain signaling role is further supported by biochemical assays that detected NADase activity required for TNL-mediated immunity (15, 16). Structural and functional studies with individual TIR domains revealed their capacity for self-association as homo- or heterodimers, which is important for immunity induction (5, 9, 17, 18). How TIR domain signaling activity is enabled by TNL effector recognition in the context of full-length receptors is unknown.

Members of the *Arabidopsis* RPP1 (Recognition of *Peronospora parasitica* 1) TNL family specifically recognize cognate ATR1 (*Arabidopsis thaliana* Recognized 1) effector variants produced by the foliar oomycete pathogen *Hyaloperonospora arabidopsidis* (*Hpa*) (19, 20). In host and pathogen populations, both RPP1 from *Arabidopsis* accessions and ATR1 from *Hpa* strains are highly polymorphic. Recognition of different ATR1 forms by RPP1 variants is *Hpa* race-specific, indicative of host-pathogen coevolution (12, 21). Specific RPP1-ATR1 recognition in *Arabidopsis* leading to leaf macroscopic host cell death was recapitulated in tobacco transient gene expression assays. Coupled with biochemical data, these studies showed a requirement for the RPP1 C-terminal LRR domain in direct binding of recognized ATR1 forms (20, 22).

Reconstitution and cryo-EM structure of the RPP1 resistosome

We coexpressed Strep-RPP1_{WsB} (residues 61 to 1221) with His-ATR1_{Emoy2} (residues 52 to 311) as a matching TNL-effector pair (12, 21) in insect cells. We used a tandem affinity purification procedure to isolate the complex. Gel

filtration analysis showed that comigration of the RPP1 and ATR1 proteins corresponded to a molecular weight of ~600 kD (fig. S1), indicating that they form an oligomeric complex, which we term the “RPP1 resistosome.” The complex obtained from gel filtration was used for structural analysis by cryo–electron microscopy (cryo-EM). After three-dimensional (3D) classification, a subset of 409,348 particles was used for image reconstruction, generating a map with a global resolution of 3.16 Å, as determined with a gold-standard Fourier shell correlation (Fig. 1A and fig. S2). Resolution of the core complex without inclusion of the LRR portion was 2.99 Å.

The cryo-EM structure of the RPP1 resistosome contains four RPP1 and four ATR1 molecules, which assemble into a tetrameric complex measuring 160 Å × 160 Å × 120 Å (Fig. 1B, fig. S3, A and B, and table S1). Tetramerization of the resistosome is mediated entirely by RPP1 subdomains. We discovered in the resistosome structure that RPP1 has a C-terminal domain in addition to the canonical TNL domains TIR, nucleotide-binding domain (NBD), helix domain 1 (HD1), winged helix domain (WHD), and LRRs (Fig. 1B and fig. S3, C to F). Structural searches of the Protein Data Bank (PDB) revealed that the C-terminal domain adopts a classical β-jelly roll and Ig-like fold (fig. S4A), which we designate C-JID (C-terminal jelly roll and Ig-like domain). The RPP1^{C-JID} structure is similar to that of the TNL Roq1 (23) (fig. S4B). Whereas all canonical TNL-type domains of RPP1 are involved in resistosome assembly, RPP1^{C-JID} mediates interaction with ATR1, assisted by the inner surface of RPP1^{LRR} (Fig. 1B). The RPP1 resistosome is organized into a three-layered ring structure, with the top, middle, and bottom formed by the TIR domain, the NOD (nucleotide-binding oligomerization domain) module (i.e., NBD-HD1-WHD domains), and ATR1-bound LRR–C-JID, respectively (Fig. 1B). RPP1^{NBD}, RPP1^{HD1}, and RPP1^{WHD} are positioned similarly to the corresponding domains of activated ZAR1, NLRC4, and Apaf-1 (fig. S4C), indicating that RPP1 adopts an active conformation in the resistosome.

RPP1^{C-JID} is an essential structural determinant for ATR1-specific recognition

RPP1-bound ATR1 is nearly identical to a crystal structure of the ATR1 monomer alone (24) (fig. S4D). RPP1^{LRR} and RPP1^{C-JID} are comparatively less well defined than other RPP1 domains (fig. S2C). The cryo-EM density of RPP1^{LRR} and RPP1^{C-JID} was substantially improved by local refinement, sufficient for model building (figs. S2C and S3, G to I). ATR1 obliquely contacts RPP1^{C-JID} and RPP1^{LRR} via its N-terminal segment (residues 67 to 190) (Fig. 2A), consistent with an earlier report that residues 68 to 222 of ATR1 are sufficient

¹Beijing Advanced Innovation Center for Structural Biology, Tsinghua-Peking Center for Life Sciences, Centre for Plant Biology, School of Life Sciences, Tsinghua University, 100084 Beijing, China. ²Max Planck Institute for Plant Breeding Research, 50829 Cologne, Germany. ³Institute of Biochemistry, University of Cologne, 50674 Cologne, Germany. ⁴Cluster of Excellence in Plant Sciences (CEPLAS), 40225 Düsseldorf, Germany.

*These authors contributed equally to this work.

†Corresponding author. Email: chai@mpipz.mpg.de (J.C.); parker@mpipz.mpg.de (J.E.P.); schlef@mpipz.mpg.de (P.S.-L.)

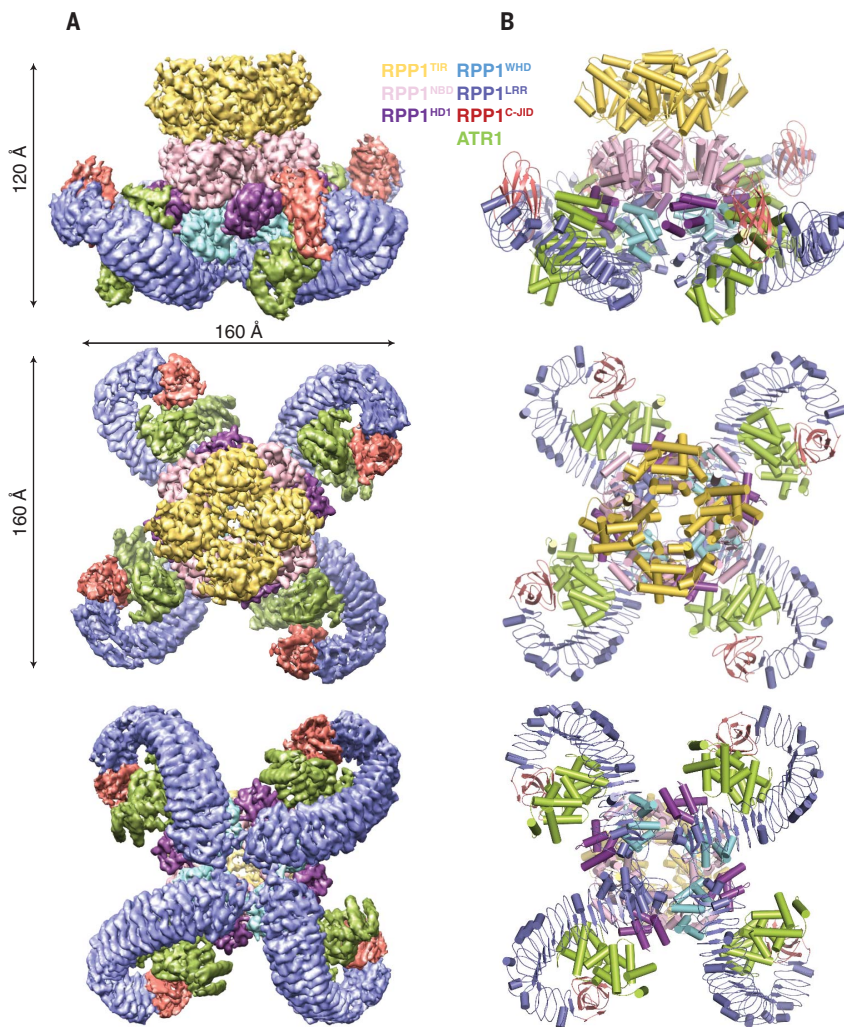


Fig. 1. Tetrameric assembly of the RPP1 resistosome. (A) Final 3D reconstruction of the RPP1 resistosome (oligomeric RPP1-ATR1 complex) in three orientations. (B) Final model of the RPP1 resistosome in three orientations. The reconstruction and model in each row are shown in the same orientation. Color codes for ATR1 and subdomains of RPP1 are indicated.

for RPP1 recognition (24). ATR1 interacts mainly with a flat exposed anti- β sheet surface of RPP1^{C-JID} (interface 1), establishing hydrogen-bonding and hydrophobic interactions (Fig. 2B and fig. S5A). Contacts with non-conserved residues from the inner surface of the curved RPP1^{LRR} further contribute to ATR1 interaction with RPP1 (interface 2) (Fig. 2C and figs. S5B and S6).

To verify the cryo-EM structure, we made substitutions of residues in ATR1 and RPP1 from interface 1 or 2, or both together. The various mutants were coexpressed in insect cells. Asp¹⁴⁰ of ATR1_Emo2 (ATR1^{D140}) that is conserved in RPP1_WsB-recognized ATR1_Maks9 and ATR1_Emco5, but not in non-recognized ATR1_Cala2 and ATR1_Emwa1 (fig. S7), is located at the center of interface 1 (Fig. 2B). Substitution of this residue with a tyrosine present at the equivalent position of ATR1_Cala2 and ATR1_Emwa1 substantially

reduced ATR1-Emoy2 binding to RPP1 in vitro (fig. S8A), indicating that interaction with RPP1^{C-JID} is important for ATR1 recognition. This result also explains why the ATR1_Cala2 and ATR1_Emwa1 alleles are not recognized by RPP1_WsB (12, 21). In further support of the cryo-EM structure, alanine substitutions of five residues from the loop region (E117A/L122A/D124A/T125A/Y126A) of ATR1 at interface 2 resulted in loss of interaction with RPP1 (fig. S8A). Substitutions of RPP1 residues at either of the two interfaces with amino acids at equivalent positions in other RPP1 variants (fig. S6) impaired interaction with ATR1_Emo2 (fig. S8A).

We tested whether the above RPP1 and ATR1 substitutions affected ATR1-induced RPP1-dependent host cell death by using *Agrobacterium tumefaciens*-mediated transient gene expression to coexpress untagged RPP1 and hemagglutinin (HA)/StrepII (HS)-

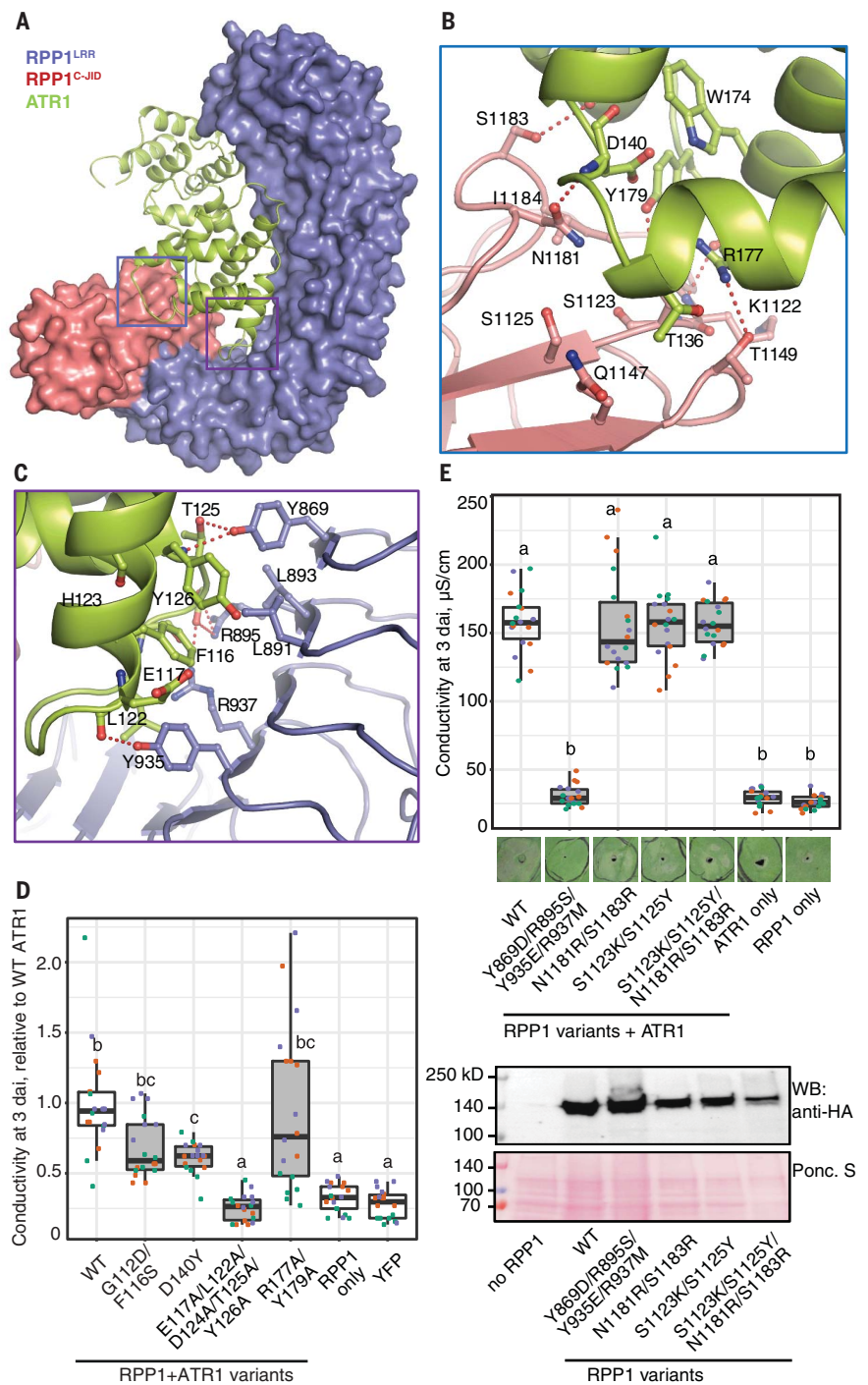
tagged ATR1 forms in leaves of *Nicotiana benthamiana*. Expectedly, coexpression of wild-type (WT) RPP1 with WT ATR1-HS resulted in cell death of infiltrated leaf zones (Fig. 2D). Epitope-tagged WT RPP1-HS also produced ATR1-dependent cell death in *N. benthamiana* and was detectable as a ~140-kD protein by immunoblotting (fig. S8, B and C). By contrast, cell death was strongly impaired with ATR1 proteins bearing substitutions that abolished or reduced interaction with RPP1 (Fig. 2, C and D, and fig. S8D). The loss of cell death induction by ATR1^{E117A/L122A/D124A/T125A/Y126A} with multiple substitutions at interface 2 (Fig. 2, C and D) showed that in addition to RPP1^{C-JID}, RPP1^{LRR} is important for ATR1 recognition, in agreement with previous data (20, 22). Coexpression of RPP1 with ATR1^{R177A/Y179A} that had no detectable interaction with RPP1 in vitro (fig. S8A) caused WT-like cell death (Fig. 2, C and D). The reason for the discrepancy remains unclear, but it is possible that a weak interaction between this ATR1 mutant and RPP1 was undetectable in vitro but was sufficient to support cell death. The RPP1 substitutions RPP1^{S1123K/S1125Y/N1181R/S1183R} from interface 1 retained WT-like cell death activity when coexpressed with ATR1, but cell death was abolished with RPP1^{Y869D/R895S/Y935E/R937M} substitutions from interface 2 (Fig. 2E). Collectively, our data indicate that RPP1^{C-JID} and RPP1^{LRR} are structural determinants for ATR1-specific binding and recognition of naturally occurring ATR1 variants. In support of this conclusion, a structure-guided RPP1 sequence alignment revealed that residues from these two domains, in particular those from RPP1^{C-JID}, are variable between different RPP1 proteins (fig. S6).

Assembly of the RPP1 resistosome is required for NADase activity

As observed in oligomerization of other NLR proteins (8, 25–27), the RPP1 central NOD module (NBD-HD1-WHD domains) participates in tetramerization (Fig. 3A and fig. S9, A and B). In contrast to other NLRs, however, the loop region between β 2 and α 2 of RPP1^{NBD} mediates RPP1 tetramerization by interacting with a groove between RPP1^{NBD} and RPP1^{WHD} of the adjacent protomer around the P-loop region (Fig. 3B and fig. S9C). Besides self-association (discussed below), the RPP1^{TIR} stacks against RPP1^{NBD} from an adjacent protomer (Fig. 3C and fig. S9, A, D, and E). Two adjacent RPP1^{TIR}s are positioned differently to engage in distinct interactions with RPP1^{NBD} (Fig. 3A). A similar observation was reported for N-terminal CARD domains in the CED-4 apoptosome (28). In the RPP1 tetramer, the TIR loop region N-terminal to RPP1^{NBD} (TIRA) is better defined than that of its neighboring TIR (TIRb). RPP1^{TIRa} packs tightly against the top

Fig. 2. Structural mechanism of ATR1 recognition by RPP1.

(A) Structure of ATR1 (in cartoon) bound by the RPP1^{LRR-C-JID} fragment (in surface) showing two interfaces with ATR1. **(B)** Detailed interactions between RPP1^{C-JID} and ATR1 at interface 1 [blue frame in (A)]. Red dashed lines indicate polar interactions. **(C)** Detailed interactions between RPP1^{LRR} and ATR1 at interface 2 [purple frame in (A)]. Red dashed lines indicate polar interactions. **(D)** Host cell death triggered by coexpression of untagged RPP1_{WsB} and HS-tagged ATR1_{Emoy2} variants in leaves of *N. benthamiana*. WT, wild type. Cell death was quantified by a leaf disk ion leakage (conductivity) assay at 3 days after agro-infiltration (dai). Data are normalized to the mean value for samples with RPP1_{WsB} and WT ATR1_{Emoy2} in each experiment. Results from three independent experiments are displayed on the plot ($n = 18$; Tukey's HSD test, $\alpha = 0.01$; data points of the same color were recorded in one experiment; shared lowercase letters indicate no significant difference). **(E)** Top: Ion leakage assay of RPP1_{WsB} mutations at RPP1-ATR1 interfaces 1 and 2 on ATR1_{Emoy2}-induced cell death in *N. benthamiana*. The assay was performed as described in (D) after agro-infiltration of C-terminally HA-StrepII-tagged RPP1_{WsB} (RPP1_{WsB}-HS) with ATR1_{Emoy2}-HS. Statistical analysis via Tukey's HSD test is based on data from three independent experiments ($n = 18$, $\alpha = 0.001$; data points of the same color were recorded in one experiment; shared lowercase letters indicate no significant difference). Below are photographs of representative agro-infiltrated leaf zones at 4 dai. Bottom: Western blot analysis of total *N. benthamiana* leaf protein extracts at 2 dai probed with antibody to HA. Expression of RPP1_{WsB}-HS WT and mutant proteins produces a signal of the expected molecular weight (~140 kD). Ponceau S staining indicates equal loading of total leaf proteins on the blot.



of RPP1^{NBD} from an adjacent protomer via extensive interactions of C-terminal parts of helices α A and α E (Fig. 3C and fig. S5C). Less tight interactions are formed between TIRb and its adjacent RPP1^{NBD} (fig. S9D). As observed in the ZARI resistosome, interactions between two neighboring LRR domains (fig. S9, A and E) likely further stabilize the RPP1 tetrameric resistosome.

We next investigated whether formation of the RPP1 resistosome is required for NADase

activity. A high-performance liquid chromatography (HPLC) assay with recombinant proteins purified from insect cells showed that the RPP1-ATR1 complex, but not RPP1 alone, hydrolyzed nicotinamide adenine dinucleotide (NAD⁺) at 1.0 μ M protein (Fig. 3D). Divalent ions were shown to be important for nucleoside hydrolase activities (29). We therefore tested whether Mg²⁺ or Ca²⁺ changed RPP1-ATR1 tetramer NAD⁺ hydrolysis. Addition of 10 mM Mg²⁺ strongly promoted consumption

of NAD⁺ by RPP1 (Fig. 3D). The same concentration of Ca²⁺ had a weaker effect. By contrast, Mg²⁺ or Ca²⁺ did not increase the negligible NADase activity of RPP1 alone (Fig. 3D). These data show that assembly of the RPP1 tetramer is necessary for NAD⁺ hydrolysis. Notably, the same concentration (1.0 μ M) of RPP1^{TIR} (residues 60 to 254) purified from insect cells was much less efficient in NAD⁺ hydrolysis (fig. S10A). At a higher concentration (70 μ M), RPP1^{TIR} NADase activity

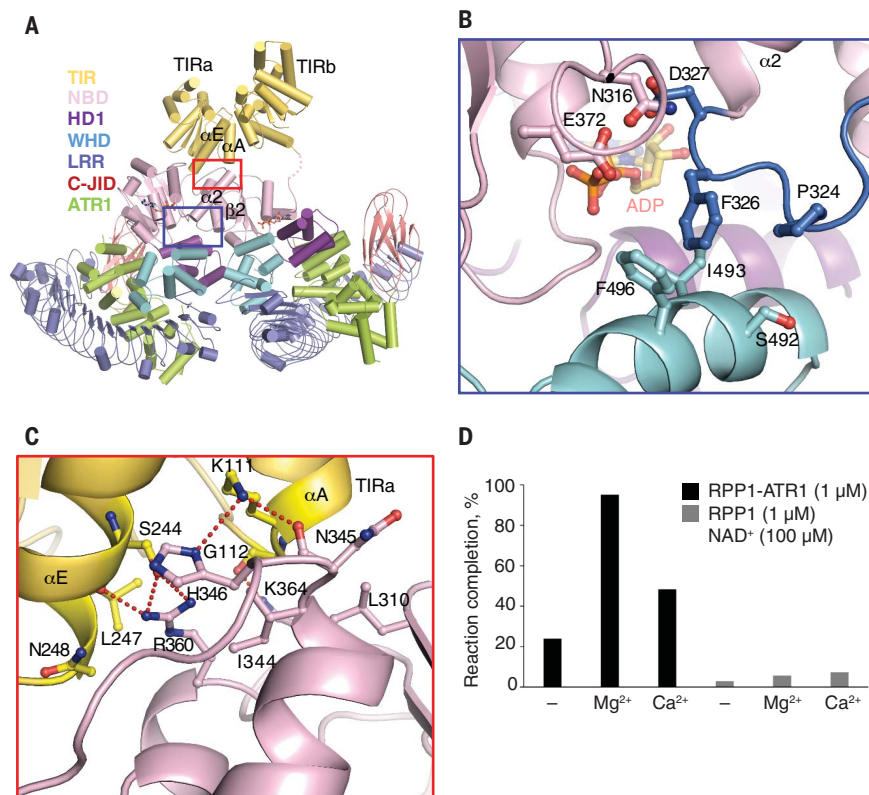


Fig. 3. The RPP1 resistosome, but not RPP1 alone, has Mg²⁺/Ca²⁺-dependent NADase activity. (A) A lateral RPP1 homodimer shown in cartoon. αA and αE are helices from the TIR domain (TIRa) in the left RPP1 protomer that interact with RPP1^{NBD} of the right protomer. The dashed line in the right RPP1 indicates the flexible region C-terminal to the TIR domains. (B) Detailed interactions of the $\beta 2$ - $\alpha 2$ loop from the right protomer with RPP1^{NBD} and RPP1^{WHD} from the left protomer highlighted within the blue frame in (A). (C) Detailed interactions between RPP1^{TIRa} and RPP1^{NBD} highlighted within the red frame in (A). (D) NADase activity assay of the ATR1-RPP1 complex and RPP1 alone. The purified ATR1-RPP1 complex or RPP1 only was incubated with 100 μM NAD⁺ in buffer with or without 10 mM Mg²⁺/Ca²⁺. After incubation at 25°C for 16 hours, reaction mixtures were centrifuged and immediately used for HPLC analysis. Reaction completion (%) of each sample was calculated as $[1 - (\text{concentration of unhydrolyzed NAD}^+)/(\text{concentration of NAD}^+ \text{ before reaction})] \times 100\%$.

was increased and promoted by Mg²⁺ and Ca²⁺ (fig. S10A), which suggests that high concentrations of TIR alone may drive it into oligomers with enzymatic activity (5). This notion is further supported by an earlier finding of RPP1^{TIR} in vivo autoactivity that correlated with its self-association in solution (30). Also, induced TIR domain proximity led to cell death in planta (31). Collectively, our data indicate that ATR1-induced assembly of the RPP1 resistosome is required for RPP1 NADase activity and host cell death induction. Thus, the RPP1 resistosome can be viewed as a pathogen-inducible holoenzyme for NAD⁺ hydrolysis.

Active sites are formed by asymmetric TIR homodimers

Whereas the four RPP1^{NOD} modules in the RPP1 resistosome are approximately related with C₄ symmetry, the four TIR domains are related with C₂ symmetry because of the dif-

ferent positioning of two neighboring RPP1^{TIR}s (Fig. 4A). Thus, the tetrameric RPP1^{TIR}s contain two symmetric TIR homodimers that are nearly identical to those observed in the crystal structure of RPP1^{TIR} (fig. S11, A and B) (18). Each of three tested substitutions of residues at this homodimeric “AE” interface (9, 17, 18) abolished ATR1-induced cell death in *N. benthamiana* (fig. S11C), supporting an essential role of the AE interface in RPP1 function. Functional relevance of the AE interface has been observed for TIR domains of other plant TNLs (9, 17, 18). In the RPP1 tetramer, opposite packing of the two symmetric TIR homodimers led to formation of two asymmetric head-to-tail RPP1^{TIR} homodimers (Fig. 4A). The two RPP1^{TIR}s in an asymmetric homodimer have different conformations in the loop between αA and αB (equivalent to the BB-loop of other TIR domains, hereafter called the BB-loop) (Fig. 4B). The BB-loop is well defined in RPP1^{TIRa} but is disordered

in RPP1^{TIRb} (fig. S12A). Asymmetric head-to-tail RPP1^{TIR}-RPP1^{TIR} interaction is primarily mediated by the BB-loop of TIRa that contacts the opposite side of TIRb (Fig. 4, A and C, and fig. S12B).

From a sequence alignment (fig. S12C), the predicted catalytic RPP1^{E158} is located at one end of the groove formed within an asymmetric RPP1^{TIR} homodimer (fig. S13A), which suggests that this groove is important for RPP1-catalyzed NAD⁺ hydrolysis and RPP1 function. To test this hypothesis, we mutated residues from the interface of the asymmetric RPP1^{TIR} homodimer and evaluated the impact of these substitutions on the NADase activity of the RPP1 resistosome and ATR1-induced cell death in *N. benthamiana*. Substitutions RPP1 I121E, S124E, A222E, or G223A, which are predicted to disrupt the asymmetric RPP1^{TIR} homodimers, all interacted with ATR1 (fig. S10B) but were strongly compromised in NAD⁺ hydrolysis (Fig. 4D and fig. S13B). By contrast, an RPP1R123A exchange had less effect on NADase activity (Fig. 4D). In support of an essential role of NADase activity in RPP1 function, we also found that RPP1 I121E, A222E, E158A, or E158Q, but not RPP1 R123A, S124E, E122A/R123A/S124A/K125A/S126A, or G223A, displayed almost undetectable cell death activity (Fig. 4E). Taken together, these data show that the assembly of two TIRa-TIRb active sites in the RPP1 resistosome is responsible for NAD⁺ hydrolysis and RPP1-mediated signaling.

A previous study showed that many single mutations in the TIR domain of the canonical *Arabidopsis* TNL RPS4 (RPS4^{TIR}) disrupted the cell death activity of RPS4^{TIR} in tobacco (13). Mapping the equivalent residues onto the RPP1 resistosome revealed that most of them cluster around the asymmetric TIRa-TIRb groove (fig. S13C). We found that adenosine triphosphate (ATP), which was supplemented during protein purification, bound to this groove in the absence of NAD⁺ (fig. S13A) and that the ATP binding groove is conserved among *Arabidopsis* TNLs (fig. S12C). The bound ATP likely acts as an analog of NAD⁺ at the groove. Supporting this possibility, a structural comparison revealed that NAD⁺ phosphate (NADP⁺) bound to the TIR domain of plant TNL RUN1 (9, 17, 18) at a position similar to that of ATP in the RPP1 TIRa-TIRb groove (fig. S13D). These results provide additional evidence for the biological relevance of the asymmetric RPP1^{TIR} homodimers in the resistosome.

ADP binds to the P-loop region of RPP1 in the resistosome

Previous studies demonstrated that structures of the NOD module from plant and animal NLRs are highly conserved in both inactive and active states (32). This is underscored here by the similar structures of RPP1^{NOD} in the

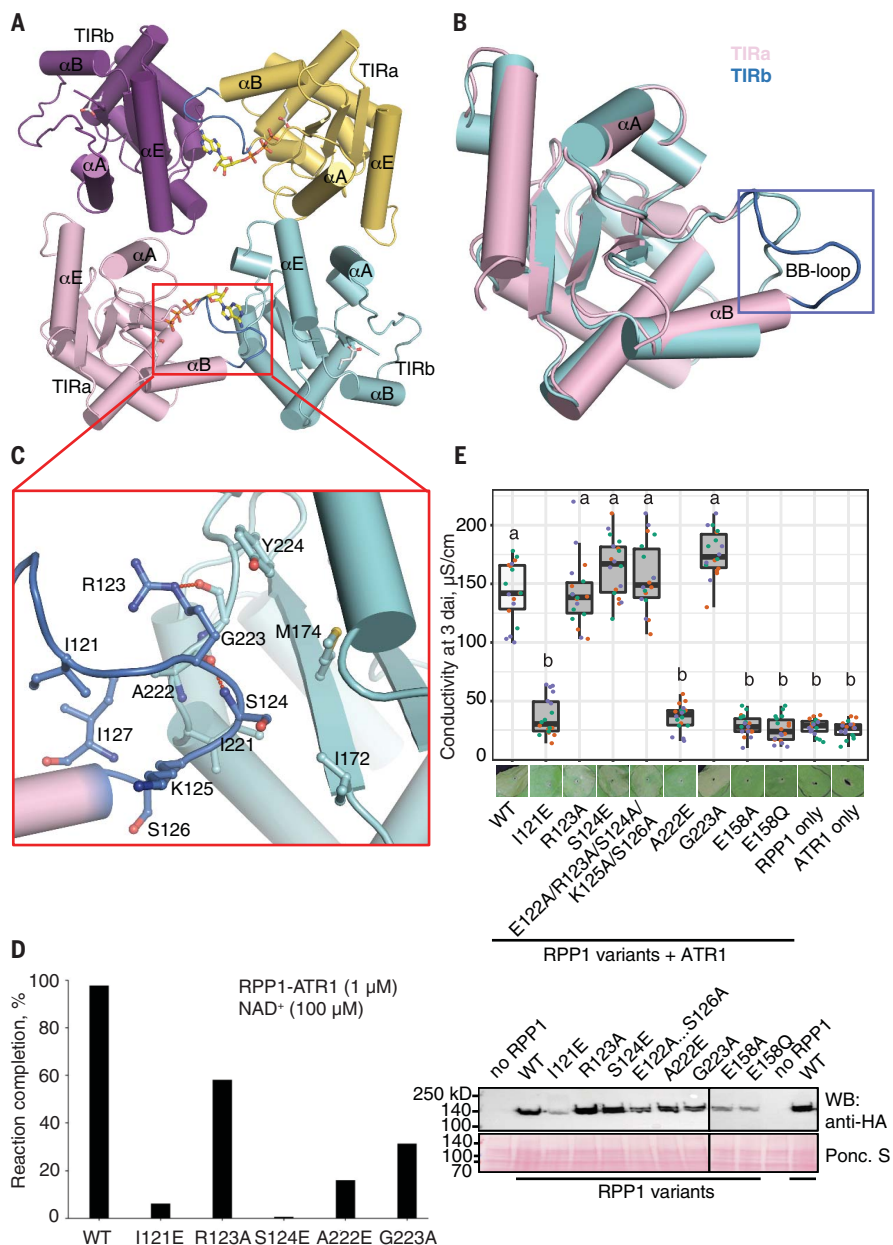


Fig. 4. Assembly of two active sites by two asymmetric RPP1^{TIR} dimers in the tetrameric RPP1 resistosome. (A) Tetrameric assembly of RPP1^{TIR}s in the resistosome. Some secondary structural elements are labeled. Two bound ATP molecules within the two asymmetric RPP1^{TIR} dimers (top and bottom dimer) are shown in stick. The loop region between αA and αB (BB-loop) from TIRa is framed in red and shown in blue. (B) Structural alignment of the two RPP1^{TIR} monomers from the asymmetric homodimer. The BB-loop from TIRa and TIRb is shown in blue and gray, respectively. The BB-loop is highlighted. (C) Detailed interactions of the BB-loop from TIRa with TIRb in the asymmetric dimer. (D) Mutagenesis analysis of the interactions shown in (C) using the NADase activity assay described in Fig. 3D. (E) Effects of mutations at sites mediating TIRa-TIRb interactions (AE interface) on RPP1_{WsB-HS} and ATR1_{Emoy2}-dependent cell death in *N. benthamiana* leaves. Host cell death was measured in a quantitative electrolyte leakage assay as described in Fig. 2. D and E. Top: Host cell death triggered by coexpression of RPP1_{WsB-HS} variants and ATR1_{Emoy2}-HS in leaves of *N. benthamiana*. Statistical analysis via Tukey's HSD test is based on data from three independent experiments ($n = 18$, $\alpha = 0.001$; data points of the same color were recorded in one experiment; shared lowercase letters indicate no significant difference). RPP1 mutants E158A and E158Q were included as additional negative controls. Below are photographs of representative agro-infiltrated leaf zones at 4 dai. Bottom: Western blot analysis of total *N. benthamiana* leaf protein extracts at 2 dai probed with antibody to HA. Expression of RPP1_{WsB-HS} WT and mutant proteins produces a signal of the expected molecular weight (~140 kD). Ponceau S staining indicates equal loading of total leaf proteins in the tested samples.

RPP1 tetramer and ZAR1^{NOD} in the ZAR1 pentamer (fig. S4C). Furthermore, NLR activation involves conformational changes in the NBD relative to its C-terminal WHD, whereas no conformational change occurs in the WHD relative to its C-terminal portion, as demonstrated in activation of ZAR1, Apaf-1, and NLRC4 (8, 25–27). A modeling study using the inactive ZAR1^{NOD} structure (33) as a template suggested that the LRR domain, in its pre-activation state, sequesters RPP1 from oligomerization, consistent with other NLR autoinhibition models (fig. S14). The modeled inactive RPP1 structure also suggested that ATR1 binding would sterically clash with RPP1^{NBD} (fig. S14B), inducing conformational changes in RPP1^{NBD} for activation. Positioning of inactive RPP1^{TIR} is difficult to predict because of the lack of a reliable template. However, overexpression of RPP1^{TIR}, but not RPP1^{TIR-NBD}, induced cell death in *N. benthamiana* (12, 30). These data point to inhibition of RPP1^{TIR} by RPP1^{NOD}, presumably through interdomain interaction similar to that observed for the inactive ZAR1^{CC} (33). An inhibitory interaction between the TIR and NBD domains was also suggested for TNLs L6 and L7 from flax (34).

On the basis of current models (5, 32), we expected an ATP molecule to be bound by the NBD of activated RPP1. Surprisingly, an adenosine diphosphate (ADP) molecule, which is unambiguously defined by the cryo-EM density, binds to the P-loop of RPP1 in the resistosome (Fig. 5A and fig. S5D). The ADP is recognized via RPP1 residues that are highly conserved in other NLR proteins (33, 35–37). Recognition of the γ -phosphate group of deoxyadenosine triphosphate (dATP)/ATP in the ZAR1 resistosome (8) and Apaf-1 apoptosome (27) is mediated through an arginine residue in a “TT/SR” motif that is essential for their activation. The arginine is highly conserved in plant CNLs and animal NLRs (38) but is substituted with a differently charged or polar residue, creating “TTE/Q” in many known TNLs including RPP1 (fig. S15, A and B). In contrast to ZAR1 and Apaf-1, however, RPP1 tolerates such substitutions, which suggests that other interactions might compensate for loss of ATP-mediated stabilization of the RPP1 resistosome. Indeed, the $\beta 2$ - $\alpha 2$ loop contributes to RPP1 oligomerization by mediating NOD-NOD interactions (Fig. 3B and Fig. 5B). In further support of this hypothesis, the TNL Roq1 with the TT/SR motif has ATP bound in its activated form and the $\beta 2$ - $\alpha 2$ loop is not involved in formation of the Roq1 resistosome (23), similar to what was observed in the ZAR1 resistosome (Fig. 5, B and C). Besides Roq1, some other TNLs also carry the TT/SR motif (fig. S15A). Most of these TNLs have a shorter $\beta 2$ - $\alpha 2$ loop relative to those without the motif (fig. S15A), providing

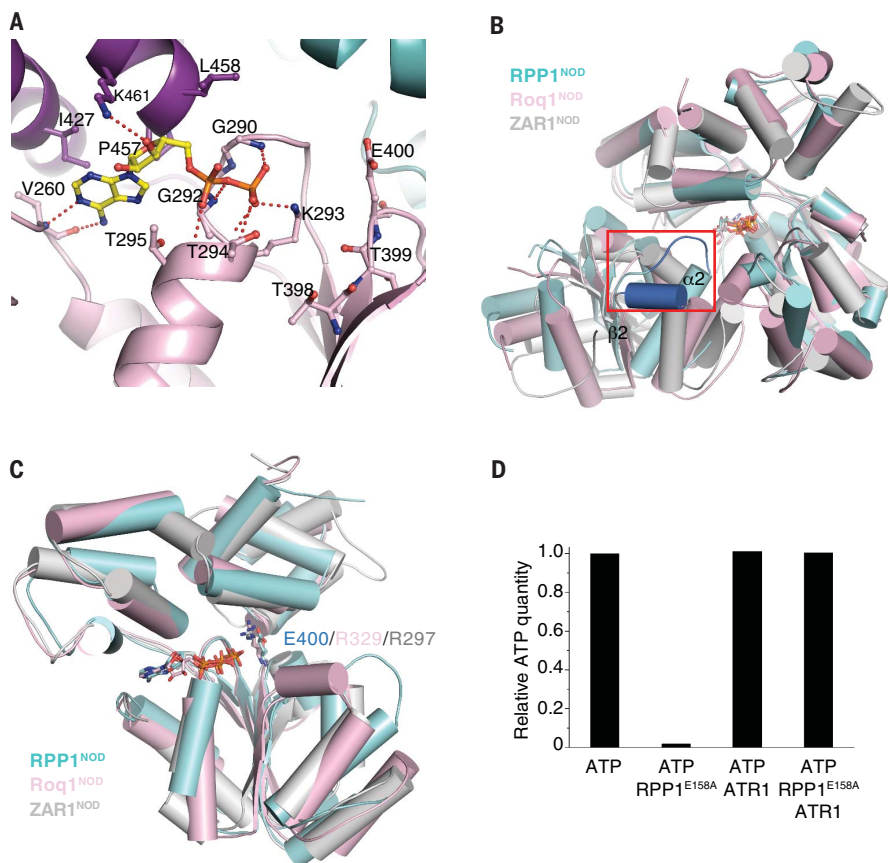


Fig. 5. Activation of RPP1 by ATR1. (A) ADP is bound between the NBD and HD1 domains in the cryo-EM structure of RPP1-ATR1. Red dashed lines represent polar interactions. A corresponding structure with EM density around the ADP-bound molecule is shown in fig. S5D. (B) Structural superposition of a lateral RPP1^{NOD} (cyan), Roq1^{NOD} (pink), and ZAR1^{NOD} (gray) homodimer. For clarity, only the NBD from the left NOD monomer is shown. The β 2- α 2 loop is shown in blue and framed in red. (C) Structural superposition of RPP1^{NOD} (cyan), Roq1^{NOD} (pink), and ZAR1^{NOD}. Arg³²⁹ and Arg²⁹⁷ from the TTR motif of Roq1 and ZAR1, respectively, and Glu⁴⁰⁰ from the equivalent position of RPP1 are indicated. The bound ADP in RPP1 and ATP in Roq1 and ZAR1 are shown in stick. (D) ATPase activity assay for RPP1^{E158A} and the RPP1^{E158A} ATR1 complex with ATR1. The recombinant proteins were individually incubated with ATP (1.0 mM) in buffer containing 10 mM Mg²⁺. After incubation at 25°C for 1 hour, samples were centrifuged and immediately used for HPLC analysis to measure ATP content. The vertical axis represents the ATP ratio after versus before the reaction.

additional evidence for the above hypothesis. Collectively, these results might explain why ADP is bound in the RPP1 tetramer, although exchange of ADP with ATP during RPP1 activation remains possible.

Bound ADP in the RPP1 resistosome might result from RPP1 intrinsic ATPase activity. To test this possibility, we used HPLC to measure the ATPase activity of the RPP1^{E158A} resistosome or nonactivated RPP1^{E158A} (to avoid potential interference from RPP1 NADase activity). In the presence of 10 mM Mg²⁺, RPP1^{E158A} alone displayed ATPase activity that was more potent than that of Apaf-1 by a factor of ~3 to 4 (Fig. 5D and fig. S16) (35, 39). In contrast, the ATR1-activated RPP1^{E158A} resistosome had much lower ATPase activity under the same conditions. Similar results were obtained with the Apaf-1 apoptosome

(39). Hence, we propose that RPP1 ATPase activity also contributes to an ADP-bound resistosome.

Discussion

We reconstituted the RPP1 resistosome and solved its structure using cryo-EM at 3.16 Å. The structure reveals the mechanism of race-specific recognition of ATR1 by RPP1, leading to NLR conformational activation. We have presented evidence for the multilayered regulation of RPP1 tetramerization, including ATR1 binding (Fig. 2), RPP1^{NOD} oligomerization (fig. S9), and RPP1^{TIR} self-association (Fig. 4). RPP1 tetramerization results in the formation of two asymmetric RPP1^{TIR} homodimers, creating active sites for NAD⁺ hydrolysis. Therefore, ATR1-induced receptor tetramerization links effector binding to the

regulation of RPP1 NADase activity. Structural and biochemical characteristics of the activated RPP1 tetramer provide a template for understanding canonical plant TIR-type NLRs.

Besides the canonical TNL domains, the C-JID that could not be predicted by primary sequence was revealed in the cryo-EM structure of the RPP1 resistosome. Biochemical and functional data show that this novel structural domain is a major determinant for specific ATR1 recognition (Fig. 2). In contrast to integrated domains of plant NLRs that are sufficient for effector recognition (7), RPP1^{C-JID} functions together with RPP1^{LRR} for specific recognition of ATR1. The sequence-diversified RPP1^{C-JID} is predicted by a hidden Markov model (HMM) to be shared by many TNLs in dicotyledonous plant species (fig. S17, A to F). It comprises part of a C-terminal domain in *Arabidopsis* TNL receptor RPS4 that confers effector-triggered immunity as a heterodimer with TNL RRS1 (17, 40). Mutations within the predicted RPS4^{C-JID} (fig. S17E) disabled RRS1/RPS4 immunity (40, 41), pointing to broader importance of the C-JID for TNL function. It is possible that the C-JID serves as a decoy that mimics common virulence targets of pathogen effectors (7). However, using HMM, we failed to detect the RPP1^{C-JID} in CNLs and non-NLR plant proteins (fig. S17, B to D). We therefore speculate that the C-JID in different TNLs plays a more generic role, together with LRRs, in TNL-specific detection of unrelated pathogen effectors. Although direct RPP1 recognition of ATR1 leads to resistosome formation, many plant NLRs perceive their cognate effectors in an indirect manner typically involving other host proteins (2).

Assembly of NADase active sites is mediated principally by the TIR BB-loop, which undergoes a major conformational change after RPP1 tetramer formation (fig. S18A). The BB-loop of RRS1^{TIR} (four residues) is shorter than that of RPP1^{TIR} and other TNL TIR domains (>9 residues; fig. S18B). The RRS1^{TIR} BB-loop in the symmetric RRS1^{TIR} homodimer or the RPS4^{TIR}-RRS1^{TIR} heterodimer (17) cannot support an RPP1^{TIR}-like asymmetric homodimer (fig. S18B). Therefore, RRS1^{TIR} would sequester the symmetric RPS4^{TIR} homodimer from self-associating into asymmetric homodimers, potentially explaining RRS1^{TIR}-mediated in planta suppression of RPS4^{TIR}-triggered cell death (17). Structural alignment reveals that the asymmetric RPP1^{TIR} homodimer is similar to that of filaments formed by MAL^{TIR} in animals (fig. S18C) (42). However, there is no experimental evidence for a filament-forming activity of RPP1^{TIR} or other plant TIR domains. Notably, MAL^{TIR} can form cofilaments with TIR domains of other proteins such as human TLR4 and MyD88 (42). Many TIR-only genes are encoded in the genome of *Arabidopsis* (43), and TNLs have

been proposed to recruit TIR-only proteins for signaling (44, 45). It will be interesting to determine whether the RPP1 resistosome can serve as a platform for interactions with TIR-only proteins or other oligomerized TNLs to amplify TNL-mediated immune signals.

Like the ZAR1 resistosome (8), the Apaf-1 apoptosome (27), and the NLRC4 inflammasome (25, 26, 46), the RPP1 tetramer forms a ring-like structure, despite the different oligomerization states of its components. The ZAR1 and RPP1 resistosomes contain, respectively, a stabilized funnel-shaped structure for plasma membrane targeting and a stabilized tetrameric RPP1^{TIR} for NADase activity. This contrasts with relatively flexible apoptosome and inflammasome N-terminal CARD domains. Hence, the N-terminal domains of plant and animal NLRs likely engage different mechanisms for immune signaling. Nonetheless, a shared principle in signaling mediated by the ZAR1 resistosome and NLRC4 inflammasome was proposed (8). The ZAR1 resistosome and probably many other CNLs with an N-terminal “MADA” motif (47) might form a membrane-resident pore or channel to mediate immunity. This is conceptually analogous to signaling mediated by the NLRC4 inflammasome that activates the pore-forming protein GSDMD for immune responses through the protease caspase-1 (48). The RPP1 resistosome, as a holoenzyme, bears similarity to both the apoptosome and the inflammasome, which form holoenzymes after recruitment of procaspase-9 and procaspase-1, respectively. Building on current models of TNL-mediated immune signaling, the RPP1 resistosome NADase activity is responsible for activation of HeLo domain-containing signaling (helper) NLRs via the EDS1 family of lipase-like proteins (49–51). It was speculated that HeLo-NLRs function similarly to ZAR1 at host membranes (8, 11, 47). Thus, the RPP1 resistosome and NLRC4 inflammasome might represent comparable paradigms in innate immunity signaling.

Materials and methods

Protein expression and purification

Sequence alignment of RPP1_WsB with its alleles RPP1_WsA, RPP1_NdA, RPP1_EstA, and RPP1_ZdrA by Clustal Omega (52) indicated that the N-terminal 60 amino acids of RPP1_WsB are not conserved. Therefore, an N-terminally truncated form of WT RPP1_WsB (61–1221) was constructed for protein expression in insect cells. ATR1_Emoy2 with an N-terminal truncation of 51 residues used for crystallization in a previous study (24) was used for protein expression. ATR1_Emoy2 (residues 52 to 311) was sufficient for recognition by RPP1, as demonstrated (24). For purification of the RPP1-ATR1 complex, a codon-optimized RPP1_WsB (61–1221; GENEWIZ

Inc.) construct was cloned into the pFastBac 1 vector (Invitrogen) with a C-terminal twin-StrepII tag. A codon-optimized ATR1_Emoy2 construct (52–311; GENEWIZ) was cloned into the pFastBac 1 vector with a C-terminal 10 × HIS tag. These constructs were coexpressed in Sf21 insect cells (Invitrogen) at 28°C. After recombinant baculovirus infection for 48 hours, infected cells were harvested and resuspended in buffer A (25 mM Tris-HCl, pH 8.0, 150 mM NaCl, 1 mM MgCl₂, and 0.3 mM ATP). After sonication and centrifugation, the RPP1-ATR1 complex was purified using Strep-Tactin resin (IBA Lifesciences) from the supernatant. Proteins bound to resin were eluted with buffer A supplemented with 2.5 mM D-thiobiotin. The eluent from Strep-Tactin was loaded onto Ni-NTA resin (Novagen) and the resin was washed with buffer A containing 20 mM imidazole. Proteins bound to the Ni-NTA resin were eluted with buffer A plus 250 mM imidazole. The eluent was concentrated through a 30-kD MWCO Vivaspin 500 concentrator (GE Healthcare) to 100 μl and loaded onto a Superose 6 increase 5/150 column (GE Healthcare) with buffer E (10 mM Tris-HCl pH 8.0, 100 mM NaCl, and 1 mM DTT). Peak fractions were concentrated to 0.45 mg/ml for cryo-EM sample preparation. A similar procedure was used for purification of the RPP1^{E158A} (61–1221)-ATR1 (52–311) complex.

Cryo-EM sample preparation and data collection

An aliquot of 3 μl of purified RPP1-ATR1 was applied to holey carbon grids (Quantifoil Au 1.2/1.3, 300 mesh) glow-discharged for 30 s at high level in Harrick Plasma after 2 min evacuation. Grids were then blotted on filter paper (Ted Pella Inc.) for 2.5 s at 8°C with 100% humidity and flash-frozen in liquid ethane using FEI Vitrobot Marked IV.

Two datasets of the WT RPP1-ATR1 complex were collected: one on a Titan Krios2 electron microscope operated at 300 kV, equipped with Gatan K3 Summit direct electron detector and a Gatan Quantum energy filter, the other on a Titan Krios3 electron microscope operated at 300 kV, equipped with a Cs-corrector, Gatan K3 Summit direct electron detector, and a Gatan Quantum energy filter. A total of 5701 and 3834 micrograph stacks were collected on Titan 2 and Titan 3, respectively. The micrograph stacks were automatically recorded using AutoEMation in superresolution mode (53), at a nominal magnification of 64,000× on Titan 2 and 81,000× on Titan 3. Defocus values varied from -1.0 μm to -2.0 μm for both datasets. Exposure rate of data collection on Titan 2 and Titan 3 was 23 and 24 electrons per pixel per second, respectively. The exposure time for both datasets was 2.56 s dose-fractionated into 32 subframes, leading to a total electron exposure of ~50 electrons per Å² for each stack.

Image processing and 3D reconstruction

The raw stacks of RPP1-ATR1 recorded in superresolution mode were motion-corrected by MotionCor2 and binned twofold, resulting in a physical pixel size of 1.0742 Å per pixel for Titan 2 motion-corrected micrographs and 1.0979 Å per pixel for Titan 3 motion-corrected micrographs (54). In the meantime, exposure rate for the summed micrographs was performed (55). Contrast transfer function (CTF) parameters were estimated by CTFFIND4 (56). Based on the CTF estimations, 5117 (Titan 2)/3123 (Titan 3) micrographs were manually picked, respectively, and were further processed in RELION3.1.

About 10,000 Laplacian-of-Gaussian auto-picked particles were subjected to 2D classification to generate initial templates for further auto-picking. For the dataset collected on Titan 2, 1,395,913 auto-picked particles were subjected to five rounds of 2D classification, which performed 25 iterations with regularization parameter $T = 2$ and number of classes = 100 to remove bad particles. Similar parameters were applied in three rounds of 2D classification of 1,125,203 auto-picked RPP1-ATR1 particles from Titan 3. After removal of bad particles, the remaining 661,434 particles on Titan 2 and 516,036 on Titan 3 for the RPP1-ATR1 complex were subjected to 3D classification with C_1 symmetry, using initial 3D reference models obtained by ab initio calculation from RELION3.1.

Particles (276,146 from Titan 2 and 133,202 from Titan 3 for RPP1-ATR1) from good 3D classes with clear overall structural features were selected for 3D refinement. At this stage, the 3D reconstructions clearly showed four RPP1 molecules in the complex. C_4 symmetry was therefore tested in the following 3D refinement. Resulting reconstructions showed that the global density, particularly that corresponding to the TIR part, became worse, indicating that lower or no symmetry exists in the RPP1-ATR1 complex. Subsequent 3D refinement with C_2 symmetry greatly improved the density quality and global resolution. After global 3D refinement with C_2 symmetry, CTF refinement, and postprocessing, the resolution of the RPP1-ATR1 reconstruction from the Titan 2 and Titan 3 datasets was 3.65 Å and 3.16 Å, respectively. Refined RPP1-ATR1 particles (409,348) from the two datasets were joined and subjected to a further round of 3D reconstruction, yielding a final cryo-EM map with 3.16 Å resolution.

A core region mask including the TIR, NBD, HD1, and WHD domains of RPP1 and ATR1 was generated by Chimera and then applied to 3D auto-refinement using C_2 symmetry and 409,348 particles from the final reconstruction with the merged datasets. In the end, the resolution of RPP1 core part reconstruction was 2.99 Å after postprocess.

The LRR and C-JID portions in the final EM map were more flexible relative to the other parts of the RPP1-ATR1 complex. To improve resolution of the local density, C_4 symmetry was first used to refine the joined particles, and the refined particles were expanded with C_4 symmetry for focused 3D classification. A local mask for LRR, C-JID, and ATR1 was generated using Chimera and then applied for focused 3D classification without alignment as described (57). After the focused 3D classification, a total of 222,015 particles were selected for C_1 focused 3D refinement, finally yielding a local reconstruction for LRR, C-JID, and ATR1 with 3.19 Å after postprocess.

2D classification, 3D classification, and 3D autorefinement were all performed with RELION3.1 (58–60). The resolutions were determined by gold-standard Fourier shell correlation (61). Local resolution distribution was evaluated using RELION (62).

Model building and refinement

The final RPP1-ATR1 EM map was generated by merging the global map and local LRR, C-JID, and ATR1 map, using combine_focused_map in PHENIX (63). For model building of the whole RPP1-ATR1 complex, the RPP1 TIR domain (PDB: 5TEB) (18) and ATR1 (PDB: 3RMR) were docked into the EM map in Chimera (64). The models of the NBD, HD1, and WHD domains of RPP1 were manually built in COOT based on the global EM map of RPP1-ATR1, and the LRR and C-JID domains in COOT using the local refined EM map (65). All the domains were then combined, generating a model containing four ATR1 molecules and four RPP1 molecules. The generated model was refined against the combined RPP1-ATR1 EM density using real-space refinement in PHENIX with secondary structure and geometry restraints (63). The final model after refinement was validated using MolProbity and EMRinger in the PHENIX package (63). Table S1 summarizes the model statistics.

In vitro NADase assays

Purified RPP1, RPP1-ATR1, mutant RPP1-ATR1, or RPP1^{TIR} were used for NADase assays at the indicated concentrations. Proteins were individually incubated with 100 μM NAD⁺ (final concentration) and 10 mM MgSO₄ or CaCl₂ in buffer containing 100 mM NaCl, 25 mM Tris-HCl pH 8.0. The total volume for each reaction was 100 μl. Reactions were performed in a thermoshaker at 25°C for 16 hours. After reaction, samples were centrifuged and immediately applied for HPLC analysis.

In vitro ATPase assays

Purified RPP1^{E158A}, RPP1^{E158A}-ATR1 complex, and ATR1 were used for ATPase assays with a protein concentration of 5 μM. Each protein was incubated with 100 μM ATP (final concentration)

in buffer containing 10.0 mM MgSO₄, 100 mM NaCl, 25.0 mM Tris-HCl pH 8.0 at 25°C for the indicated times. The volume for reaction was 100 μl. After reaction, samples were centrifuged and immediately applied for HPLC analysis. 1.0 μM RPP1^{E158A} was used to quantify its ATPase activity. Reactions were carried out as described above. Samples (50 μl) taken at different time points (1, 2, 3, 4, and 5 hours) were analyzed on an HPLC system to detect the formed ADP. By comparison with reference samples (ADP), the respective integrated ADP peak area was converted into concentration. The ATPase activity was calculated by five data points-based linear regression.

HPLC measurements

HPLC was performed on an Agilent 1260 bioinert HPLC system using a Synergi Fusion-RP 80 Å (4.6 × 150 mm, 4 μm) (Phenomenex) column. The samples were measured via an 8-min method. Samples (10 μl) were injected at 550 μl/min with ammonium formate (5 mM) in water and methanol used as mobile phases A and B, respectively. The elution profile was as follows: 0 to 3 min, 10 to 70% B; 3 to 6 min, 70% B; 6 to 6.1 min, 70 to 10% B; 6.1 to 8 min, 10% B. The autosampler temperature was maintained at 4°C and the column temperature at 25°C. UV signals were detected at 260 nm. Reference standards were used to determine respective retention times. The integrations of peak area were used to calculate relative concentrations.

Site-directed mutagenesis of RPP1_WsB and ATR1_Emoy2 for in planta analyses

For *N. benthamiana* transient expression analyses, the RPP1_WsB gene body (exons and introns) was PCR-amplified from the pENTR/D-TOPO pRPP1:gRPP1 construct provided by K. Krasileva (12, 19) and cloned into pENTR/D-TOPO vector (Thermo Fisher Scientific, K240020). The ATR1_Emoy2 sequence starts with a codon corresponding to T19 in NCBI accession AAX51198 ATR1_Emoy2, thereby removing a signal peptide. Mutagenesis was performed using a QuikChange II site-directed mutagenesis kit (Agilent, 200523) or KOD-Plus-Mutagenesis kit (CosmoBio, SMK-101). Sequences of oligonucleotides are provided in table S2. Obtained pENTR/D-TOPO RPP1_WsB and pDONR207 ATR1_Emoy2 plasmids were LR-recombined (Thermo Fisher Scientific, 11791020) into pXCSG vectors (66) to allow expression of untagged RPP1^{WsB}, C-terminally tagged RPP1_WsB-3xHA-StrepII, and ATR1_Emoy2-3xHA-StrepII proteins under a 35S promoter. All constructs were verified by DNA sequencing. Generated binary constructs were transformed into *Agrobacterium tumefaciens* (*Rhizobium radiobacter*) GV3101 pMP90RK via electroporation.

Protein expression in *N. benthamiana* and Western blot analysis

RPP1_WsB-HS and ATR1_Emoy2-HS were expressed in *N. benthamiana* using agrobacteria-mediated transient expression assays in the presence of the P19 suppressor of RNAi silencing as in (49). The final OD₆₀₀ for each strain was set to 0.2. To detect ATR1 variants, two 8-mm leaf discs per sample were harvested at 2 dai and boiled at 95°C in Laemmli buffer for 5 min. The ATR1-HS fusions were blotted onto nitrocellulose membranes and detected using primary α-HA antibodies (Sigma Aldrich, 11867423001 or H6908; Cell Signaling Technology, #3724) and secondary horseradish peroxidase (HRP)-conjugated antibodies (Santa Cruz, sc-2006; Sigma Aldrich, A5164) at dilution 1:5000 (3% milk powder in TBST). Detection was performed using enhanced chemiluminescence assays Clarity, Clarity Max Western ECL (Bio-Rad, #1705061 and #1705062). To detect RPP1_WsB-HS variants, infiltrated *N. benthamiana* leaves were collected at 2 dai, frozen in liquid nitrogen, and ground to a fine powder. Powder (~100 μl in a tube) was resuspended in 100 μl of urea-SDS sample buffer [50 mM Tris-HCl pH 6.8, 2% SDS, 8 M urea, 2% β-mercaptoethanol, 5% glycerol, protease inhibitor cocktail (Roche), and 0.004% Bromophenol Blue] and vortexed for 10 min at room temperature. No boiling step was included. After centrifugation at 16,000g for 10 min, 10 μl of the supernatant was loaded onto 8% SDS-PAGE and proteins were blotted onto a PVDF membrane. Immunoblot assay was performed using monoclonal rat anti-HA antibody (Sigma Aldrich, 11867423001) diluted 1:4000 and rabbit anti-rat antibody (Sigma Aldrich, A5164) diluted 1:5000 in 1× TBS, 0.1% Tween-20 with 3.5% w/v nonfat dry milk. RPP1_WsB-HS fusion proteins were detected using ECL SuperSignal West Femto Maximum Sensitivity Substrate and ECL Western Blotting substrate (Thermo Scientific) in a ratio of 2:1.

Cell death quantification in *N. benthamiana*

RPP1_WsB-HS and ATR1_Emoy2-HS WT and mutant protein combinations were transiently expressed in *N. benthamiana* as described above (49) and agrobacteria-infiltrated leaf zones used for cell death (ion leakage) assays at 3 dai as described (49). Statistical analysis was performed on conductivity data normalized to the mean level in samples containing WT RPP1_WsB and ATR1_Emoy2 samples via Tukey's HSD (honestly significant difference) test after checking normality of residuals distribution and homogeneity of variance using visual examination of the plots and Shapiro-Wilcoxon and Levene tests ($P > 0.05$). Images of agrobacteria-infiltrated leaf spots were taken at 4 to 5 dpi.

RPPI_WsB jelly roll/Ig-like (JID) sequence distribution across plants

Protein sequences of 32 representative plant species from green algae to *Arabidopsis thaliana* were obtained as in (49). Sequences similar to the jelly roll domain of RPPI_WsB (amino acids 1075 to 1195) were initially searched with BLASTP (-evalue 0.01). The jelly roll-like sequences were detected at this step only in *Brassicaceae* plants. The match sequences were extracted and aligned via the Muscle method. A hidden Markov model was built from the resulting alignment [hmmbuild in HMMER 3.1b2 (67), default settings]. This model (v1) identified 622 matches mainly in Brassicales but also in Fabales, Malpighiales, and Rosales (Reference Proteomes 2020_04, hmmsearch at EMBL-EBI-incE 0.01). To improve sensitivity of the search, a next version of the HMM model was prepared. For that, the v1 HMM was run against the 32 species protein database above (hmmsearch in HMMER 3.1b2, -incE 0.01) and not against public databases to avoid with redundancy and skewing toward *Brassicaceae* in public databases. The resulting matches were again extracted, aligned with Clustal Omega, and the obtained alignment served as an input for building the version 2 HMM, available as data S1. The v2 HMM run against Uniprot database (2019-10-03) at EMBL-EBI (hmmsearch -E1-domE 1-incE 0.001-incdomE 0.03-seqdb uniprotkb) identified 2711 hits, only in eudicots. The majority of found proteins have a typical TNL domain architecture, other hits have different arrangements/combinations of NBARC, LRR, TIR domains and occasionally other domains. Finally, to assess distribution of the RPPI_WsB-like JID across plants, the v2 HMM (data S1) was scanned against the above custom non-redundant database of protein sequences from 32 representative plant species (hmmsearch-incE 0.01).

REFERENCES AND NOTES

- H. Burdett, B. Kobe, P. A. Anderson, Animal NLRs continue to inform plant NLR structure and function. *Arch. Biochem. Biophys.* **670**, 58–68 (2019). doi: [10.1016/j.abb.2019.05.001](https://doi.org/10.1016/j.abb.2019.05.001); pmid: [31071301](https://pubmed.ncbi.nlm.nih.gov/31071301/)
- J. D. Jones, R. E. Vance, J. L. Dangl, Intracellular innate immune surveillance devices in plants and animals. *Science* **354**, aaf6395 (2016). doi: [10.1126/science.aaf6395](https://doi.org/10.1126/science.aaf6395); pmid: [27934708](https://pubmed.ncbi.nlm.nih.gov/27934708/)
- S. Lolle, D. Stevens, G. Coaker, Plant NLR-triggered immunity: From receptor activation to downstream signaling. *Curr. Opin. Immunol.* **62**, 99–105 (2020). doi: [10.1016/j.coi.2019.12.007](https://doi.org/10.1016/j.coi.2019.12.007); pmid: [31958770](https://pubmed.ncbi.nlm.nih.gov/31958770/)
- T. Maekawa, T. A. Kufer, P. Schulze-Lefert, NLR functions in plant and animal immune systems: So far and yet so close. *Nat. Immunol.* **12**, 817–826 (2011). doi: [10.1038/ni.2083](https://doi.org/10.1038/ni.2083); pmid: [21852785](https://pubmed.ncbi.nlm.nih.gov/21852785/)
- S. Nimma, T. Ve, S. J. Williams, B. Kobe, Towards the structure of the TIR-domain signalosome. *Curr. Opin. Struct. Biol.* **43**, 122–130 (2017). doi: [10.1016/j.sbi.2016.12.014](https://doi.org/10.1016/j.sbi.2016.12.014); pmid: [28092811](https://pubmed.ncbi.nlm.nih.gov/28092811/)
- J. Wang, J. Chai, Molecular actions of NLR immune receptors in plants and animals. *Sci. China Life Sci.* **63**, 1–14 (2020). doi: [10.1007/s11427-019-1687-6](https://doi.org/10.1007/s11427-019-1687-6); pmid: [32613490](https://pubmed.ncbi.nlm.nih.gov/32613490/)
- E. Grund, D. Tremoussaygue, L. Deslandes, Plant NLRs with Integrated Domains: Unity Makes Strength. *Plant Physiol.* **179**, 1227–1235 (2019). doi: [10.1104/pp.18.01134](https://doi.org/10.1104/pp.18.01134); pmid: [30530739](https://pubmed.ncbi.nlm.nih.gov/30530739/)
- J. Wang et al., Reconstitution and structure of a plant NLR resistosome conferring immunity. *Science* **364**, eaav5870 (2019). doi: [10.1126/science.aav5870](https://doi.org/10.1126/science.aav5870); pmid: [30948527](https://pubmed.ncbi.nlm.nih.gov/30948527/)
- M. Bernoux et al., Structural and functional analysis of a plant resistance protein TIR domain reveals interfaces for self-association, signaling, and autoregulation. *Cell Host Microbe* **9**, 200–211 (2011). doi: [10.1016/j.chom.2011.02.009](https://doi.org/10.1016/j.chom.2011.02.009); pmid: [21402359](https://pubmed.ncbi.nlm.nih.gov/21402359/)
- S. Cesari et al., Cytosolic activation of cell death and stem rust resistance by cereal MLA-family CC-NLR proteins. *Proc. Natl. Acad. Sci. U.S.A.* **113**, 10204–10209 (2016). doi: [10.1073/pnas.1605483113](https://doi.org/10.1073/pnas.1605483113); pmid: [27555587](https://pubmed.ncbi.nlm.nih.gov/27555587/)
- S. M. Collier, L. P. Hamel, P. Moffett, Cell death mediated by the N-terminal domains of a unique and highly conserved class of NB-LRR protein. *Mol. Plant Microbe Interact.* **24**, 918–931 (2011). doi: [10.1094/MPMI-03-11-0050](https://doi.org/10.1094/MPMI-03-11-0050); pmid: [21501087](https://pubmed.ncbi.nlm.nih.gov/21501087/)
- K. V. Krasileva, D. Dahlbeck, B. J. Staskawicz, Activation of an Arabidopsis resistance protein is specified by the in planta association of its leucine-rich repeat domain with the cognate oomycete effector. *Plant Cell* **22**, 2444–2458 (2010). doi: [10.1105/tpc.110.075358](https://doi.org/10.1105/tpc.110.075358); pmid: [20601497](https://pubmed.ncbi.nlm.nih.gov/20601497/)
- M. R. Swiderski, D. Birker, J. D. Jones, The TIR domain of TIR-NB-LRR resistance proteins is a signaling domain involved in cell death induction. *Mol. Plant Microbe Interact.* **22**, 157–165 (2009). doi: [10.1094/MPMI-22-2-0157](https://doi.org/10.1094/MPMI-22-2-0157); pmid: [19132868](https://pubmed.ncbi.nlm.nih.gov/19132868/)
- T. Maekawa et al., Coiled-coil domain-dependent homodimerization of intracellular barley immune receptors defines a minimal functional module for triggering cell death. *Cell Host Microbe* **9**, 187–199 (2011). doi: [10.1016/j.chom.2011.02.008](https://doi.org/10.1016/j.chom.2011.02.008); pmid: [21402358](https://pubmed.ncbi.nlm.nih.gov/21402358/)
- L. Wan et al., TIR domains of plant immune receptors are NAD⁺-cleaving enzymes that promote cell death. *Science* **365**, 799–803 (2019). doi: [10.1126/science.aax1771](https://doi.org/10.1126/science.aax1771); pmid: [31439793](https://pubmed.ncbi.nlm.nih.gov/31439793/)
- S. Horsefield et al., NAD⁺ cleavage activity by animal and plant TIR domains in cell death pathways. *Science* **365**, 793–799 (2019). doi: [10.1126/science.aax1911](https://doi.org/10.1126/science.aax1911); pmid: [31439792](https://pubmed.ncbi.nlm.nih.gov/31439792/)
- S. J. Williams et al., Structural basis for assembly and function of a heterodimeric plant immune receptor. *Science* **344**, 299–303 (2014). doi: [10.1126/science.1247357](https://doi.org/10.1126/science.1247357); pmid: [24744375](https://pubmed.ncbi.nlm.nih.gov/24744375/)
- X. Zhang et al., Multiple functional self-association interfaces in plant TIR domains. *Proc. Natl. Acad. Sci. U.S.A.* **114**, E2046–E2052 (2017). doi: [10.1073/pnas.1621248114](https://doi.org/10.1073/pnas.1621248114); pmid: [28159890](https://pubmed.ncbi.nlm.nih.gov/28159890/)
- M. A. Botella et al., Three genes of the Arabidopsis RPPI complex resistance locus recognize distinct *Peronospora parasitica* avirulence determinants. *Plant Cell* **10**, 1847–1860 (1998). doi: [10.1105/tpc.10.11.1847](https://doi.org/10.1105/tpc.10.11.1847); pmid: [9811793](https://pubmed.ncbi.nlm.nih.gov/9811793/)
- A. D. Steinbrenner, S. Goritschnig, B. J. Staskawicz, Recognition and activation domains contribute to allele-specific responses of an Arabidopsis NLR receptor to an oomycete effector protein. *PLoS Pathog.* **11**, e1004665 (2015). doi: [10.1371/journal.ppat.1004665](https://doi.org/10.1371/journal.ppat.1004665); pmid: [25671309](https://pubmed.ncbi.nlm.nih.gov/25671309/)
- A. P. Rehmany et al., Differential recognition of highly divergent downy mildew avirulence gene alleles by RPPI resistance genes from two Arabidopsis lines. *Plant Cell* **17**, 1839–1850 (2005). doi: [10.1105/tpc.105.031807](https://doi.org/10.1105/tpc.105.031807); pmid: [15894715](https://pubmed.ncbi.nlm.nih.gov/15894715/)
- S. Goritschnig, A. D. Steinbrenner, D. J. Grunwald, B. J. Staskawicz, Structurally distinct Arabidopsis thaliana NLR immune receptors recognize tandem WY domains of an oomycete effector. *New Phytol.* **210**, 984–996 (2016). doi: [10.1111/nph.13823](https://doi.org/10.1111/nph.13823); pmid: [26725254](https://pubmed.ncbi.nlm.nih.gov/26725254/)
- R. Martin et al., Structure of the activated Roq1 resistosome directly recognizing the pathogen effector HopQ. bioRxiv 246413 [preprint]. 14 August 2020.
- S. Chou et al., Hyaloperonospora arabidopsidis ATR1 effector is a repeat protein with distributed recognition surfaces. *Proc. Natl. Acad. Sci. U.S.A.* **108**, 13323–13328 (2011). doi: [10.1073/pnas.1109791108](https://doi.org/10.1073/pnas.1109791108); pmid: [21788488](https://pubmed.ncbi.nlm.nih.gov/21788488/)
- Z. Hu et al., Structural and biochemical basis for induced self-propagation of NLRC4. *Science* **350**, 399–404 (2015). doi: [10.1126/science.aac5489](https://doi.org/10.1126/science.aac5489); pmid: [26449475](https://pubmed.ncbi.nlm.nih.gov/26449475/)
- L. Zhang et al., Cryo-EM structure of the activated NAIP2-NLRC4 inflammasome reveals nucleated polymerization. *Science* **350**, 404–409 (2015). doi: [10.1126/science.aac5789](https://doi.org/10.1126/science.aac5789); pmid: [26449474](https://pubmed.ncbi.nlm.nih.gov/26449474/)
- M. Zhou et al., Atomic structure of the apoptosome: Mechanism of cytochrome c- and dATP-mediated activation of Apaf-1. *Genes Dev.* **29**, 2349–2361 (2015). doi: [10.1101/gad.272278.115](https://doi.org/10.1101/gad.272278.115); pmid: [26543158](https://pubmed.ncbi.nlm.nih.gov/26543158/)
- S. Qi et al., Crystal structure of the Caenorhabditis elegans apoptosome reveals an octameric assembly of CED-4. *Cell* **141**, 446–457 (2010). doi: [10.1016/j.cell.2010.03.017](https://doi.org/10.1016/j.cell.2010.03.017); pmid: [20434985](https://pubmed.ncbi.nlm.nih.gov/20434985/)
- T. Ogawa, Y. Ueda, K. Yoshimura, S. Shigeoka, Comprehensive analysis of cytosolic Nudix hydrolases in Arabidopsis thaliana. *J. Biol. Chem.* **280**, 25277–25283 (2005). doi: [10.1074/jbc.M503536200](https://doi.org/10.1074/jbc.M503536200); pmid: [15878881](https://pubmed.ncbi.nlm.nih.gov/15878881/)
- K. J. Schreiber, A. Bentham, S. J. Williams, B. Kobe, B. J. Staskawicz, Multiple Domain Associations within the Arabidopsis Immune Receptor RPPI Regulate the Activation of Programmed Cell Death. *PLoS Pathog.* **12**, e1005769 (2016). doi: [10.1371/journal.ppat.1005769](https://doi.org/10.1371/journal.ppat.1005769); pmid: [27427964](https://pubmed.ncbi.nlm.nih.gov/27427964/)
- Z. Duxbury et al., Induced proximity of a TIR signaling domain on a plant-mammalian NLR chimera activates defense in plants. *Proc. Natl. Acad. Sci. U.S.A.* **117**, 18832–18839 (2020). doi: [10.1073/pnas.2001185117](https://doi.org/10.1073/pnas.2001185117); pmid: [32709746](https://pubmed.ncbi.nlm.nih.gov/32709746/)
- Y. Xiong, Z. Han, J. Chai, Resistosome and inflammasome: Platforms mediating innate immunity. *Curr. Opin. Plant Biol.* **56**, 47–55 (2020). doi: [10.1016/j.pbi.2020.03.010](https://doi.org/10.1016/j.pbi.2020.03.010); pmid: [32554225](https://pubmed.ncbi.nlm.nih.gov/32554225/)
- J. Wang et al., Ligand-triggered allosteric ADP release primes a plant NLR complex. *Science* **364**, eaav5868 (2019). doi: [10.1126/science.aav5868](https://doi.org/10.1126/science.aav5868); pmid: [30948526](https://pubmed.ncbi.nlm.nih.gov/30948526/)
- M. Bernoux et al., Comparative Analysis of the Flax Immune Receptors L6 and L7 Suggests an Equilibrium-Based Switch Activation Model. *Plant Cell* **28**, 146–159 (2016). doi: [10.1105/tpc.15.00303](https://doi.org/10.1105/tpc.15.00303); pmid: [26744216](https://pubmed.ncbi.nlm.nih.gov/26744216/)
- Z. Hu et al., Crystal structure of NLRC4 reveals its autoinhibition mechanism. *Science* **341**, 172–175 (2013). doi: [10.1126/science.1236381](https://doi.org/10.1126/science.1236381); pmid: [23765277](https://pubmed.ncbi.nlm.nih.gov/23765277/)
- H. Sharif et al., Structural mechanism for NEK7-licensed activation of NLPR3 inflammasome. *Nature* **570**, 338–343 (2019). doi: [10.1038/s41586-019-1295-z](https://doi.org/10.1038/s41586-019-1295-z); pmid: [31189953](https://pubmed.ncbi.nlm.nih.gov/31189953/)
- J. F. C. Steele, R. K. Hughes, M. J. Banfield, Structural and biochemical studies of an NB-ARC domain from a plant NLR immune receptor. *PLoS ONE* **14**, e0221226 (2019). doi: [10.1371/journal.pone.0221226](https://doi.org/10.1371/journal.pone.0221226); pmid: [31461469](https://pubmed.ncbi.nlm.nih.gov/31461469/)
- X. Yang, G. Lin, Z. Han, J. Chai, Structural Biology of NOD-Like Receptors. *Adv. Exp. Med. Biol.* **1172**, 119–141 (2019). doi: [10.1007/978-981-13-9367-9_6](https://doi.org/10.1007/978-981-13-9367-9_6); pmid: [31628654](https://pubmed.ncbi.nlm.nih.gov/31628654/)
- T. F. Reubold, S. Wohlgemuth, S. Eschenburg, A new model for the transition of APAF-1 from inactive monomer to caspase-activating apoptosome. *J. Biol. Chem.* **284**, 32717–32724 (2009). doi: [10.1074/jbc.M109.014027](https://doi.org/10.1074/jbc.M109.014027); pmid: [19801675](https://pubmed.ncbi.nlm.nih.gov/19801675/)
- Y. Ma et al., Distinct modes of depression of an Arabidopsis immune receptor complex by two different bacterial effectors. *Proc. Natl. Acad. Sci. U.S.A.* **115**, 10218–10227 (2018). doi: [10.1073/pnas.1811858115](https://doi.org/10.1073/pnas.1811858115); pmid: [30254172](https://pubmed.ncbi.nlm.nih.gov/30254172/)
- K. H. Sohn et al., The nuclear immune receptor RPS4 is required for RRS1SLH1-dependent constitutive defense activation in Arabidopsis thaliana. *PLoS Genet.* **10**, e1004655 (2014). doi: [10.1371/journal.pgen.1004655](https://doi.org/10.1371/journal.pgen.1004655); pmid: [25340333](https://pubmed.ncbi.nlm.nih.gov/25340333/)
- T. Ve et al., Structural basis of TIR-domain-assembly formation in MAL- and MyD88-dependent TLR4 signaling. *Nat. Struct. Mol. Biol.* **24**, 743–751 (2017). doi: [10.1038/nsmb.3444](https://doi.org/10.1038/nsmb.3444); pmid: [28759049](https://pubmed.ncbi.nlm.nih.gov/28759049/)
- B. C. Meyers, M. Morgante, R. W. Michelmore, TIR-X and TIR-NBS proteins: Two new families related to disease resistance TIR-NBS-LRR proteins encoded in Arabidopsis and other plant genomes. *Plant J.* **32**, 77–92 (2002). doi: [10.1046/j.1365-3113.X.2002.01404.x](https://doi.org/10.1046/j.1365-3113.X.2002.01404.x); pmid: [12366802](https://pubmed.ncbi.nlm.nih.gov/12366802/)
- R. S. Nandety et al., The role of TIR-NBS and TIR-X proteins in plant basal defense responses. *Plant Physiol.* **162**, 1459–1472 (2013). doi: [10.1104/pp.113.219162](https://doi.org/10.1104/pp.113.219162); pmid: [23735504](https://pubmed.ncbi.nlm.nih.gov/23735504/)
- M. T. Nishimura et al., TIR-only protein RBA1 recognizes a pathogen effector to regulate cell death in Arabidopsis. *Proc. Natl. Acad. Sci. U.S.A.* **114**, E2053–E2062 (2017). doi: [10.1073/pnas.1620973114](https://doi.org/10.1073/pnas.1620973114); pmid: [28137883](https://pubmed.ncbi.nlm.nih.gov/28137883/)
- J. L. Tenthorey et al., The structural basis of flagellin detection by NAIP5: A strategy to limit pathogen immune evasion. *Science* **358**, 888–893 (2017). doi: [10.1126/science.aal1140](https://doi.org/10.1126/science.aal1140); pmid: [29146805](https://pubmed.ncbi.nlm.nih.gov/29146805/)
- H. Adachi et al., An N-terminal motif in NLR immune receptors is functionally conserved across distantly related plant species. *eLife* **8**, e49956 (2019). doi: [10.7554/eLife.49956](https://doi.org/10.7554/eLife.49956); pmid: [31774397](https://pubmed.ncbi.nlm.nih.gov/31774397/)
- L. Wang, H. Wu, Keeping the Death Protein in Check. *Immunity* **51**, 1–2 (2019). doi: [10.1016/j.immuni.2019.06.011](https://doi.org/10.1016/j.immuni.2019.06.011); pmid: [31315028](https://pubmed.ncbi.nlm.nih.gov/31315028/)

49. D. Lapin *et al.*, A Coevolved EDS1-SAG101-NRG1 Module Mediates Cell Death Signaling by TIR-Domain Immune Receptors. *Plant Cell* **31**, 2430–2455 (2019). doi: [10.1105/tpc.19.00118](https://doi.org/10.1105/tpc.19.00118); pmid: [31311833](https://pubmed.ncbi.nlm.nih.gov/31311833/)
50. B. Castel *et al.*, Diverse NLR immune receptors activate defence via the RPW8-NLR NRG1. *New Phytol.* **222**, 966–980 (2019). doi: [10.1111/nph.15659](https://doi.org/10.1111/nph.15659); pmid: [30582759](https://pubmed.ncbi.nlm.nih.gov/30582759/)
51. Z. Wu *et al.*, Differential regulation of TNL-mediated immune signaling by redundant helper CNLs. *New Phytol.* **222**, 938–953 (2019). doi: [10.1111/nph.15665](https://doi.org/10.1111/nph.15665); pmid: [30585636](https://pubmed.ncbi.nlm.nih.gov/30585636/)
52. F. Sievers *et al.*, Fast, scalable generation of high-quality protein multiple sequence alignments using Clustal Omega. *Mol. Syst. Biol.* **7**, 539 (2011). doi: [10.1038/msb.2011.75](https://doi.org/10.1038/msb.2011.75); pmid: [21988835](https://pubmed.ncbi.nlm.nih.gov/21988835/)
53. J. Lei, J. Frank, Automated acquisition of cryo-electron micrographs for single particle reconstruction on an FEI Tecnai electron microscope. *J. Struct. Biol.* **150**, 69–80 (2005). doi: [10.1016/j.jsb.2005.01.002](https://doi.org/10.1016/j.jsb.2005.01.002); pmid: [15797731](https://pubmed.ncbi.nlm.nih.gov/15797731/)
54. S. Q. Zheng *et al.*, MotionCor2: Anisotropic correction of beam-induced motion for improved cryo-electron microscopy. *Nat. Methods* **14**, 331–332 (2017). doi: [10.1038/nmeth.4193](https://doi.org/10.1038/nmeth.4193); pmid: [28250466](https://pubmed.ncbi.nlm.nih.gov/28250466/)
55. T. Grant, N. Grigorieff, Measuring the optimal exposure for single particle cryo-EM using a 2.6 Å reconstruction of rotavirus VP6. *eLife* **4**, e06980 (2015). doi: [10.7554/eLife.06980](https://doi.org/10.7554/eLife.06980); pmid: [26023829](https://pubmed.ncbi.nlm.nih.gov/26023829/)
56. J. A. Mindell, N. Grigorieff, Accurate determination of local defocus and specimen tilt in electron microscopy. *J. Struct. Biol.* **142**, 334–347 (2003). doi: [10.1016/S1047-8477\(03\)00069-8](https://doi.org/10.1016/S1047-8477(03)00069-8); pmid: [12781660](https://pubmed.ncbi.nlm.nih.gov/12781660/)
57. X. C. Bai, E. Rajendra, G. Yang, Y. Shi, S. H. Scheres, Sampling the conformational space of the catalytic subunit of human γ -secretase. *eLife* **4**, e11182 (2015). doi: [10.7554/eLife.11182](https://doi.org/10.7554/eLife.11182); pmid: [26623517](https://pubmed.ncbi.nlm.nih.gov/26623517/)
58. S. H. Scheres, RELION: Implementation of a Bayesian approach to cryo-EM structure determination. *J. Struct. Biol.* **180**, 519–530 (2012). doi: [10.1016/j.jsb.2012.09.006](https://doi.org/10.1016/j.jsb.2012.09.006); pmid: [23000701](https://pubmed.ncbi.nlm.nih.gov/23000701/)
59. S. H. Scheres, A Bayesian view on cryo-EM structure determination. *J. Mol. Biol.* **415**, 406–418 (2012). doi: [10.1016/j.jmb.2011.11.010](https://doi.org/10.1016/j.jmb.2011.11.010); pmid: [22100448](https://pubmed.ncbi.nlm.nih.gov/22100448/)
60. J. Zivanov, T. Nakane, S. H. W. Scheres, Estimation of high-order aberrations and anisotropic magnification from cryo-EM data sets in RELION-3.1. *IUCr* **7**, 253–267 (2020). doi: [10.1107/S2052252520000081](https://doi.org/10.1107/S2052252520000081); pmid: [32148853](https://pubmed.ncbi.nlm.nih.gov/32148853/)
61. P. B. Rosenthal, R. Henderson, Optimal determination of particle orientation, absolute hand, and contrast loss in single-particle electron cryomicroscopy. *J. Mol. Biol.* **333**, 721–745 (2003). doi: [10.1016/j.jmb.2003.07.013](https://doi.org/10.1016/j.jmb.2003.07.013); pmid: [14568533](https://pubmed.ncbi.nlm.nih.gov/14568533/)
62. A. Kucukelbir, F. J. Sigworth, H. D. Tagare, Quantifying the local resolution of cryo-EM density maps. *Nat. Methods* **11**, 63–65 (2014). doi: [10.1038/nmeth.2727](https://doi.org/10.1038/nmeth.2727); pmid: [24213166](https://pubmed.ncbi.nlm.nih.gov/24213166/)
63. P. D. Adams *et al.*, PHENIX: A comprehensive Python-based system for macromolecular structure solution. *Acta Crystallogr. D* **66**, 213–221 (2010). doi: [10.1107/S0907444909052925](https://doi.org/10.1107/S0907444909052925); pmid: [20124702](https://pubmed.ncbi.nlm.nih.gov/20124702/)
64. E. F. Pettersen *et al.*, UCSF Chimera—A visualization system for exploratory research and analysis. *J. Comput. Chem.* **25**, 1605–1612 (2004). doi: [10.1002/jcc.20084](https://doi.org/10.1002/jcc.20084); pmid: [15264254](https://pubmed.ncbi.nlm.nih.gov/15264254/)
65. P. Emsley, B. Lohkamp, W. G. Scott, K. Cowtan, Features and development of Coot. *Acta Crystallogr. D* **66**, 486–501 (2010). doi: [10.1107/S0907444910007493](https://doi.org/10.1107/S0907444910007493); pmid: [20383002](https://pubmed.ncbi.nlm.nih.gov/20383002/)
66. C. P. Witte, L. D. Noël, J. Gielbert, J. E. Parker, T. Romeis, Rapid one-step protein purification from plant material using the eight-amino acid StrepII epitope. *Plant Mol. Biol.* **55**, 135–147 (2004). doi: [10.1007/s1103-004-0501-y](https://doi.org/10.1007/s1103-004-0501-y); pmid: [15604670](https://pubmed.ncbi.nlm.nih.gov/15604670/)
67. S. R. Eddy, Accelerated Profile HMM Searches. *PLOS Comput. Biol.* **7**, e1002195 (2011). doi: [10.1371/journal.pcbi.1002195](https://doi.org/10.1371/journal.pcbi.1002195); pmid: [22039361](https://pubmed.ncbi.nlm.nih.gov/22039361/)

ACKNOWLEDGMENTS

We thank J. Lei, X. Li, X. Fan, and N. Liu at Tsinghua University for data collection. We acknowledge the Tsinghua University Branch of the China National Center for Protein Sciences (Beijing) for

providing the cryo-EM facility support and the computational facility support on the cluster of Bio-Computing Platform.

Funding: Supported by the National Natural Science Foundation of China (31421001 to J.C. and 31971119 to Z.H.), the Alexander von Humboldt Foundation (a Humboldt professorship to J.C.), the Max-Planck-Gesellschaft (J.E.P. and P.S.-L., and a Max Planck fellowship to J.C.), Deutsche Forschungsgemeinschaft SFB-1403-414786233 (J.C., J.E.P., and P.S.-L.) and Germany's Excellence Strategy CEPLAS (EXC-2048/1, Project 390686111) (J.C., J.E.P., and P.S.-L.). **Author contributions:** Experimental design: J.C., J.E.P., P.S.-L., S.M., D.L.; recombinant protein expression assays, purification, structure determinations, modeling, and data analysis: S.M., X.Z., Y.S., W.S., J.W., and J.C.; biochemical assays: S.M., W.S., D.Y., J.J., Z.H.; plant expression and cell death assays: L.L., D.L., E.L.; HMM building: D.L.; data analysis: all authors; manuscript writing: J.C., J.E.P., P.S.-L. with contributions from other authors. **Competing interests:** The authors declare no competing interests. **Data and materials availability:** Plasmids for in planta expression of RPP1_WsB and ATR1_Emo2 variants (table S2) are available from J.E.P. or P.S.-L. under a material agreement with Max Planck Institute for Plant Breeding Research. All data are available in the main text, supplementary materials, or the listed Protein Data Bank (PDB) files. For the RPP1 resistosome and RPP1RR-C-JID-ATR1, the atomic coordinates have been deposited in the PDB with accession codes 7CRC and 7CRB, respectively. The EM maps have been deposited in the Electron Microscopy Database with accession codes EMD-30450 and EMD-30449, respectively.

SUPPLEMENTARY MATERIALS

science.sciencemag.org/content/370/6521/eabe3069/suppl/DC1
Figs. S1 to S18
Tables S1 and S2
Data S1
References (68–71)

13 August 2020; accepted 22 October 2020
[10.1126/science.abe3069](https://doi.org/10.1126/science.abe3069)

Direct pathogen-induced assembly of an NLR immune receptor complex to form a holoenzyme

Shoucai Ma, Dmitry Lapin, Li Liu, Yue Sun, Wen Song, Xiaoxiao Zhang, Elke Logemann, Dongli Yu, Jia Wang, Jan Jirschitzka, Zhifu Han, Paul Schulze-Lefert, Jane E. Parker and Jijie Chai

Science **370** (6521), eabe3069.
DOI: 10.1126/science.abe3069

Tetrameric immune receptors

Nucleotide-binding/leucine-rich repeat (NLR) immune receptors detect pathogen effectors and trigger a plant's immune response. Two groups have now defined the structures of two NLRs that carry Toll-like interleukin-1 receptor (TIR) domains (TIR-NLRs) (see the Perspective by Tian and Li). Ma *et al.* studied the *Arabidopsis thaliana* TIR-NLR RPP1 (recognition of *Peronospora parasitica* 1) and its response to effectors from an oomycete pathogen. Martin *et al.* studied the *Nicotiana benthamiana* TIR-NLR ROQ1 (recognition of XopQ 1) and its response to the *Xanthomonas* effector. Both groups found that these TIR-NLRs formed tetramers that, when activated by binding to the pathogen effector, exposed the active site of a nicotinamide adenine dinucleoside (NAD) hydrolase. Thus, recognition of the pathogen effector initiates NAD hydrolysis and begins the immune response.

Science, this issue p. eabe3069, p. eabd9993; see also p. 1163

ARTICLE TOOLS

<http://science.sciencemag.org/content/370/6521/eabe3069>

SUPPLEMENTARY MATERIALS

<http://science.sciencemag.org/content/suppl/2020/12/02/370.6521.eabe3069.DC1>

RELATED CONTENT

<http://science.sciencemag.org/content/sci/370/6521/1163.full>
<http://science.sciencemag.org/content/sci/370/6521/eabd9993.full>

REFERENCES

This article cites 69 articles, 26 of which you can access for free
<http://science.sciencemag.org/content/370/6521/eabe3069#BIBL>

PERMISSIONS

<http://www.sciencemag.org/help/reprints-and-permissions>

Use of this article is subject to the [Terms of Service](#)

Science (print ISSN 0036-8075; online ISSN 1095-9203) is published by the American Association for the Advancement of Science, 1200 New York Avenue NW, Washington, DC 20005. The title *Science* is a registered trademark of AAAS.

Copyright © 2020 The Authors, some rights reserved; exclusive licensee American Association for the Advancement of Science. No claim to original U.S. Government Works